A 2.5D BEM-based approach in the Bézier-Bernstein space for railway noise prediction and acoustic barrier assessment

R. Velázquez-Mata[1,*], C. Knuth[2], A. Romero[1], G. Squicciarini[2], A. Tadeu[3,4], D.J. Thompson[2],
P. Galvín[1,5]

[1] *Escuela Técnica Superior de Ingeniería, Universidad de Sevilla, Camino de los Descubrimientos, ES-41092, Spain*
[2] *ISVR, University of Southampton, Highfield, Southampton, SO17 1BJ, UK*
[3] *University of Coimbra, CERIS, Department of Civil Engineering, Pólo II, Rua Luís Reis Santos, 3030-788 Coimbra, Portugal*
[4] *Itecons, Institute of Research and Technological Development in Construction, Energy, Environment and Sustainability, Rua Pedro Hispano, 3030-289 Coimbra, Portugal*
[5] *ENGREEN, Laboratory of Engineering for Energy and Environmental Sustainability, Universidad de Sevilla, Camino de los Descubrimientos s/n, ES-41092, Spain*

Abstract

Noise pollution from railway traffic, primarily caused by rolling noise resulting from the vibrations of the track and wheels, is a major public health concern. While traditional acoustic barriers are effective, they are often visually intrusive, particularly in urban settings. This has led to growing interest in more integrated solutions, such as low, close barriers, which require accurate noise prediction tools. This paper presents a two-and-a-half-dimensional BEM for predicting and mitigating railway noise. The method uses Bézier-Bernstein space to accurately model complex geometries, enhancing noise prediction across different rail profiles. Several rail configurations are compared to evaluate their impact on noise emissions and to support the design of more effective and adaptable barrier solutions. The method is then applied to evaluate the performance of a specific low-height barrier configuration, considering the presence of the vehicle to assess its impact on noise reduction. Numerical predictions are validated through comparison with experimental data and other numerical approaches. Results highlight the importance of accurate source modelling for barrier design and demonstrate the potential of the proposed method as a flexible tool for developing noise mitigation solutions that utilise the barrier's geometry to improve acoustic performance and support visual integration in urban environments.

Keywords: rolling noise, acoustic barriers, Bézier-Bernstein geometry, Boundary Element Method, railway noise mitigation

---

Email address: `rvmata@us.es` (R. Velázquez-Mata[1,*])

Preprint submitted to Engineering Analysis with Boundary Elements *26 November 2025*

1. Introduction

Environmental noise is an important issue that can have a profound impact on the health of citizens. Noise pollution is therefore controlled through regulations and guidelines that utilise engineering tools and urban planning [1]. In railway traffic, various factors remain a concern and continue to be the subject of ongoing research. For example, He et al. [2] numerically investigated the aerodynamic noise from a high-speed train bogie, identifying the shear layer detached from the upstream components as a critical contributor to noise generation, particularly at lower frequencies. Castellini et al. [3] studied squeal noise in tramway sharp curves, showing that additional flange back contact can alter excitation conditions and promote mode coupling. Torstensson et al. [4] analysed impact noise at railway crossings using a hybrid model, showing that reducing the effective dip angle can significantly lower wheel-rail impact loads and radiated noise.

However, the primary contributor to environmental noise pollution from railways is rolling noise [5]. This noise is generated by the vibrations of the track and wheels, which are excited by surface irregularities. Numerous authors have studied this phenomenon. Thompson et al.[6] developed the TWINS model under the ERRI C163 committee to predict wheel/rail rolling noise, integrating theoretical approaches and validating it through full-scale tests using measured surface roughness and pass-by acoustic data. In a subsequent study, Thompson et al. [7] investigated three distinct methodologies to separate the noise contributions originating from the train wheels and the track during a pass-by event. While both components—wheel and rail—radiate noise, the rail often dominates at lower speeds, which are typical when trains traverse urban areas. In such settings, where dense populations are most affected, noise mitigation becomes a priority. Underground railways are often the preferred solution to reduce both acoustic and environmental disruptions. However, when subterranean construction is not feasible, alternative measures must be implemented. While traditional acoustic barriers are effective at reducing noise, they are expensive and often introduce visual intrusions disrupting the urban landscape. This requires innovative strategies, such as low-height acoustic barriers [5], which aim not only to mitigate noise effectively but also to integrate railway lines into the urban environment harmoniously. The effectiveness of acoustic barriers depends on factors such as their location, height, length, acoustic absorption, noise source, and soil surface properties. Several methodologies to determine the properties of acoustic barriers have been standardised [8–14], and their design has been the subject of extensive research over the years [15]. In 1969, Rathe [16] presented measured barrier attenuation near the tracks of a railway line. Later, Kurze and Anderson [17] compared these results with those obtained by diffraction theory. Makarewicz et al. [18] proposed expressions for the sound pressure level and sound exposure level of a passing train assuming that geometrical spreading was the major factor influencing the propagation of the noise.

Recently, Micheli and Farné [19] proposed an advanced approach to support decision making in noise reduction intervention by evaluating the minimum cost. A case study was performed in a rail noise-affected urban cluster, examining parameters such as the size of the buildings, the level of railway traffic, the cost of the acoustic barriers, etc. The study concluded that acoustic barriers were the most cost-effective measure compared to insulated windows. In contrast, Oertli [20] asserts that railway noise control is most cost effective when addressing noise at the source through technical improvements such as low noise brakes and wheel maintenance, rather than relying on passive measures like barriers or facade insulation. Redondo et al. [21] compared sound insulation and noise barrier insertion loss with the perception of annoyance reduction using surveys of people of two different nationalities. Lee et al. [22] presented measurements of several housing estates to investigate the effect of noise barriers on the mitigation of train noise. Fiorini [23] assessed the sound levels generated by the railway infrastructure and proposed measures to mitigate noise pollution.

The design of the barrier is usually analysed by numerical models. Tadeu and collaborators [24] have studied the problem in depth using the boundary element method (BEM), the hypersingular formulation of the BEM, and a coupling approach, both using the so-called dual methodology. A key step in reducing computational cost in three-dimensional sound propagation simulations around noise barriers involves transforming the 3D problem into a series of two-dimensional problems solved for real and imaginary frequencies using a boundary element mesh. This approach was originally proposed by Duhamel et al. [25] and has since been adopted and further developed by other researchers under the name two-and-a-half-dimensional (2.5D) methodology. For instance, Godinho et al. [26] applied this 2.5D BEM approach to evaluate acoustic scattering by an infinitely long rigid non-absorbing barrier near tall buildings, analysing sound pressure reduction and shadow zone effects. Tadeu et al. [24] computed the sound pressure attenuation caused by thin rigid screens installed on tall building walls to shield them from direct sound incidence by nearby sources, simulating wave propagation around screens of various sizes and geometries. António et al. [27] modeled 3D wave propagation around two-dimensional rigid acoustic screens, with minimal thickness, placed in a fluid layer. Later, Tadeu et al. [28] used a dual BEM formulation to model the propagation of sound generated by fixed and moving point loads in 2.5D configurations, in the presence of very thin elements with partially absorbing surfaces. The model was verified against closed-form solutions. António et al. [29] simulated the propagation of sound generated by point pressure sources in the vicinity of double 3D barriers, placed so as to create an indoor acoustic space. The authors analysed different barrier shape geometries and their relative positions with respect to a lateral wall to evaluate the performance of double 3D rigid barriers creating an acoustic space.

More researchers have dedicated their efforts to understanding the behaviour of acoustic barriers. Bordón et al. [30] developed a 2D BEM-finite element method (FEM) model to analyse sound barriers. Later, Toledo et al. [31] presented a procedure for optimizing the discrete shape of barrier top devices featuring thick and very thin bodies conceived as null-thickness types, using dual BEM. In References [32, 33], they studied the improvement in acoustic barrier efficiency by optimizing the designs of top-edge devices in terms of screening performance. Li et al. [34] presented a scale modelling method to measure the acoustic performance of a nearly enclosed barrier and the corresponding predictions using a 2.5D BEM. The measured results and the numerical calculations were in good agreement and they concluded that the 2.5D BEM formulation can provide a reliable description of the acoustic performance of a nearly-enclosed barrier. Li et al. [35] introduced statistical energy analysis (SEA) to predict the insertion loss of vertical noise barrier on railway bridges, evaluating the barrier performance for different heights, structural styles, and material composition. Lázaro et al. [36] studied a low-height acoustic barrier for use close to the noise source in a railway environment through numerical modelling with the BEM.

Many models have been developed to simulate sound propagation around railway infrastructure, often relying on coupled FEM-BEM formulations that require meshing the entire track domain. This increases computational cost and complexity, especially for high-frequency analyses. Additionally, these models often fail to represent Computer Aided Design (CAD) geometries accurately and rely on standard numerical integration and low element orders. The integration of isogeometric analysis (IGA) with BEM has been investigated in several works, motivated by the need for more accurate and efficient acoustic simulations. Peake et al. [37] proposed an extended IGA-BEM (XIBEM) for two-dimensional Helmholtz problems, combining partition-of-unity enrichment with Non-Uniform Rational B-Splines (NURBS)-based geometry representation to achieve highly accurate solutions with fewer degrees of freedom. Simpson et al. [38] employed a T-spline based IGA-BEM to integrate CAD design directly with boundary element analysis, demonstrating superior accuracy in low-frequency acoustic problems. Liu et al. [39] introduced a fast multipole IGA-BEM for two-dimensional acoustics and a sensitivity-based shape optimization of sound barriers, highlighting efficient geometry control and computational performance. Jiang et al. [40] presented a combined shape and topology optimization method for sound barriers using IGA-BEM, employing control points for geometry and artificial densities for sound-absorbing material distribution. The present work proposes a 2.5D Boundary Element Method formulated in the Bézier-Bernstein space, which enables exact CAD-level geometry representation, and applies the QUEEN [41] quadrature rule for the integration. The method supports arbitrary high-order elements, improving both accuracy and computational efficiency in high-frequency noise prediction.

This paper presents a boundary element method formulation to evaluate the noise generated by different track systems. The versatility of the numerical model enables the analysis of barriers with different shapes, thereby maximising the noise mitigation. Defining the geometry of the barrier, however, first requires an accurate evaluation of the noise generated by the specific track system in each case. The model also enables the analysis of complex geometries in track system components, such as rails and other structural elements, providing a complete understanding of the system's acoustic behaviour.

The paper is organised as follows. First, the numerical model is briefly described. Next, the model is validated through an experimental test conducted at the University of Southampton [42], followed by a comparison with results from another numerical model developed by Knuth et al. [43]. These validations provide a robust foundation for analysing several cases of different track systems subjected to a vertical point load, comparing their responses in terms of point and transfer mobility and sound power. Following this, different geometries of acoustic barriers are introduced to assess their effectiveness in mitigating noise, with a comparison of the results before and after their implementation. Finally, the presence of a railway vehicle is incorporated into the analysis, examining its impact on noise dispersion and mitigation, and evaluating how its inclusion influences the overall acoustic performance.

2. Numerical formulation

A domain Ω, which includes the track system and the air medium, is divided into separate subdomains, as shown in the example in Figure 1. These subdomains comprise the solid regions, consisting of the rail (Ω_{s_1}) and the rail pad (Ω_{s_2}), as well as the air medium (Ω_f). The number of solid subdomains is not limited, allowing the inclusion of as many components as necessary to represent a specific track system accurately. Additionally, acoustic barriers can be incorporated into the model at any desired location, as well as the boundary of the railway vehicle, to assess their influence on noise radiation. All subdomains are modelled using the Boundary Element Method. Assuming the problem is invariant along the z-direction, the solution is calculated in the frequency-wavenumber $\omega - \kappa_z$ domain using a two-and-a-half-dimensional (2.5D) approach [44]:

$$\mathbf{a}(\mathbf{x}, \omega) = \int_{-\infty}^{+\infty} \widetilde{\mathbf{a}}(\widetilde{\mathbf{x}}, \kappa_z, \omega) e^{-\iota \kappa_z z} \, d\kappa_z \tag{1}$$

where $\widetilde{\mathbf{a}}(\widetilde{\mathbf{x}}, \kappa_z, \omega)$ is the frequency-wavenumber representation of a variable of interest (e.g., displacement or sound pressure), ω is the angular frequency, assuming time dependence of the form $\exp(\iota\omega t)$, $\mathbf{x} = \mathbf{x}(x, y, z)$ and $\widetilde{\mathbf{x}} = \mathbf{x}(x, y, 0)$. The Greek letter ι denotes the unit imaginary number.

The solution of the coupled air-track system is obtained by imposing appropriate conditions at the solid-solid and solid-fluid interfaces. Equilibrium of forces and compatibility of displacements must be achieved at solid interfaces; and the equilibrium of normal pressure, with null shear stress, and continuity of normal displacement are imposed at the solid-fluid interface Γ_{sf}. Each subdomain is directly coupled, and the equations are assembled into a global system.

2.1. Boundary element formulation in elastodynamics

Solids in track systems such as rail and rail pad are represented using the BEM formulation in elastodynamics. The integral representation of the displacement $\widetilde{\mathbf{u}}_i$ for a point i, with zero body forces and zero initial conditions, may be written as [45]:

$$\mathbf{c}_i(\widetilde{\mathbf{x}}_i)\widetilde{\mathbf{u}}_i(\widetilde{\mathbf{x}}_i, \kappa_z, \omega) = \int_{\Gamma_s} \Big(\widetilde{\mathbf{t}}(\widetilde{\mathbf{x}}, \kappa_z, \omega)\widetilde{\mathcal{G}}(\widetilde{\mathbf{x}}, \kappa_z, \omega; \widetilde{\mathbf{x}}_i) - \widetilde{\mathbf{u}}(\widetilde{\mathbf{x}}, \kappa_z, \omega)\widetilde{\mathcal{H}}(\widetilde{\mathbf{x}}, \kappa_z, \omega; \widetilde{\mathbf{x}}_i) \Big) \, d\Gamma(\widetilde{\mathbf{x}}) \tag{2}$$

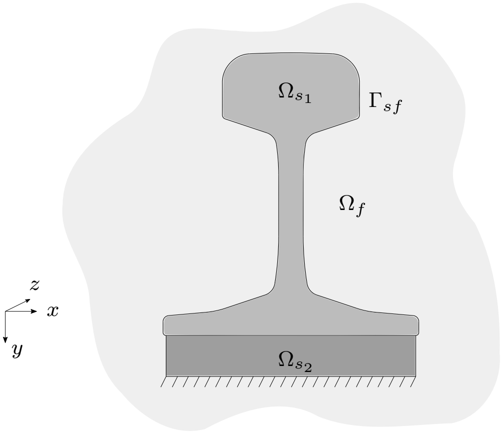

Figure 1: Boundary subdomains definition: rail (Ω_{s_1}), rail pad (Ω_{s_2}) and air medium (Ω_f).

where $\widetilde{\mathbf{u}}(\widetilde{\mathbf{x}}, \kappa_z, \omega)$ and $\widetilde{\mathbf{t}}(\widetilde{\mathbf{x}}, \kappa_z, \omega)$ are displacement and traction, respectively. $\widetilde{\mathcal{G}}(\widetilde{\mathbf{x}}, \kappa_z, \omega; \widetilde{\mathbf{x}}_i)$ and $\widetilde{\mathcal{H}}(\widetilde{\mathbf{x}}, \kappa_z, \omega; \widetilde{\mathbf{x}}_i)$ are the full-space fundamental solution for displacement and traction at the point $\widetilde{\mathbf{x}}$ due to a point source acting at the collocation point $\widetilde{\mathbf{x}}_i$. The integral-free term $\mathbf{c}_i(\widetilde{\mathbf{x}}_i)$ depends only on the boundary geometry at the collocation point $\widetilde{\mathbf{x}}_i$.

The two-and-a-half-dimensional Green's function is obtained using the potentials $\tilde{A}_p$ and $\tilde{A}_s$ for the irrotational and equivoluminal parts of the displacement vector, respectively [46]:

$$\tilde{A}_p = \frac{\iota}{4\rho\omega^2}\left[H_0^{(2)}(\kappa_\alpha r) - H_0^{(2)}(-\iota\kappa_z r)\right] \tag{3}$$

$$\tilde{A}_s = \frac{\iota}{4\rho\omega^2}\left[H_0^{(2)}(\kappa_\beta r) - H_0^{(2)}(-\iota\kappa_z r)\right] \tag{4}$$

where $\kappa_\alpha = \sqrt{\kappa_p^2 - \kappa_z^2}$ and $\kappa_\beta = \sqrt{\kappa_s^2 - \kappa_z^2}$, and κ_p and κ_s represent the wavenumbers for dilatational and shear waves, respectively. $H_0^{(2)}$ is the Hankel function of the second kind and $r = \sqrt{x^2 + y^2}$. Thus, the displacement $\widetilde{\mathcal{G}}_{kl}(\widetilde{\mathbf{x}}, \kappa_z, \omega; \widetilde{\mathbf{x}}_i)$ in the k direction at $\widetilde{\mathbf{x}}$ due to a point load acting in the l direction at $\widetilde{\mathbf{x}}_i$ is obtained from:

$$\widetilde{\mathcal{G}}_{kl}(\widetilde{\mathbf{x}}, \kappa_z, \omega; \widetilde{\mathbf{x}}_i) = \frac{\partial^2(\tilde{A}_p - \tilde{A}_s)}{\partial x_k \partial x_l} + \delta_{kl}\tilde{\nabla}^2 \tilde{A}_s \tag{5}$$

2.2. Boundary element formulation in fluid-acoustics

The integral representation of the sound pressure in the frequency-wavenumber domain for a point $\widetilde{\mathbf{x}}_i$ located at the boundary Γ_{sf} can be written as [44]:

$$c_i(\widetilde{\mathbf{x}}_i)\widetilde{p}_i(\widetilde{\mathbf{x}}_i, \kappa_z, \omega) = -\int_{\Gamma_{sf}} \left(\iota\rho\omega\widetilde{v}(\widetilde{\mathbf{x}}, \kappa_z, \omega)\widetilde{\Psi}(\widetilde{\mathbf{x}}, \kappa_z, \omega; \widetilde{\mathbf{x}}_i) + \widetilde{p}(\widetilde{\mathbf{x}}, \kappa_z, \omega)\frac{\partial\widetilde{\Psi}(\widetilde{\mathbf{x}}, \kappa_z, \omega; \widetilde{\mathbf{x}}_i)}{\partial\mathbf{n}}\right) d\Gamma(\widetilde{\mathbf{x}}) \tag{6}$$

where $\widetilde{p}(\widetilde{\mathbf{x}}, \kappa_z, \omega)$ and $\widetilde{v}(\widetilde{\mathbf{x}}, \kappa_z, \omega)$ are the sound pressure and the particle normal velocity at the boundary Γ_{sf}, respectively. $\widetilde{\Psi}(\widetilde{\mathbf{x}}, \kappa_z, \omega; \widetilde{\mathbf{x}}_i)$ represents the velocity potential at point $\widetilde{\mathbf{x}}$ due to a point source located at $\widetilde{\mathbf{x}}_i$:

$$\widetilde{\Psi}(\widetilde{\mathbf{x}}, \kappa_z, \omega; \widetilde{\mathbf{x}}_i) = -\frac{\imath}{4} H_0^{(2)}(\kappa_f r) \tag{7}$$

where $\kappa_f = \sqrt{(\omega/c_f)^2 - \kappa_z^2}$ is the fluid wavenumber, c_f is the sound propagation speed, and $H_0^{(2)}$ is the Hankel function of the second kind.

2.3. Geometry and element approximation

The BEM formulations presented in the previous sections are implemented in the Bézier-Bernstein space [44]. The Bézier-Bernstein formulation of the BEM enables a geometry-independent field approximation. The proposed method is geometrically exact, based on Computer Aided Design (CAD), but field variables are independently approximated from the geometry. We use the Bézier-Bernstein form of a polynomial as an approximation basis to represent both geometry and field variables. The application of Bernstein polynomials for the representation of a Bézier curve $\mathbf{r}_n(t)$ is:

$$\mathbf{r}_n(t) = \sum_{k=0}^{n} \mathbf{b}_k B_k^n(t) \tag{8}$$

where $\mathbf{b}_k$ are the control points used to approximate the geometry and n is the curve degree. An efficient curve computation is achieved using the polar form (or blossom) of a Bézier curve $\mathbf{r}_n(t)$, which defines a multiaffine transformation satisfying:

$$\mathbf{b}_k = \mathbf{R}(\underbrace{0, \ldots, 0}_{n-k}, \underbrace{1, \ldots, 1}_{k}) \tag{9}$$

where $\mathbf{R}(t_1, \ldots, t_n)$ is computed as:

$$\mathbf{R}(t_1, \ldots, t_n) = \sum_{\substack{I \cap J = \emptyset \\ I \cup J = \{1,2,\ldots,n\}}} \prod_{i \in I} (1 - t_i) \prod_{j \in J} t_j \mathbf{b}_{|J|} \tag{10}$$

Thus, a Bernstein polynomial can be formulated in polar form substituting Equation (9) into Equation (8) as follows:

$$\mathbf{r}_n(t) = \sum_{k=0}^{n} \mathbf{R}(\underbrace{0, \ldots, 0}_{n-k}, \underbrace{1, \ldots, 1}_{k}) B_k^n(t) = \mathbf{R}(t, \ldots, t) \tag{11}$$

The Bézier-Bernstein space is used to describe the exact element geometry as $\Gamma^j(\mathbf{x}) = \mathbf{r}_n^j(t)$. Hence, the element integrals can be written on the univariate basis $t \in [0, 1]$ as [44]:

$$\int_{\Gamma^j} f(\widetilde{\mathbf{x}}, \kappa_z, \omega; \widetilde{\mathbf{x}}_i)\, d\Gamma = \int_0^1 f(\widetilde{\mathbf{x}}(t), \kappa_z, \omega; \widetilde{\mathbf{x}}_i) \left| \frac{d\mathbf{r}_n^j(t)}{dt} \right| dt \tag{12}$$

where $f(\widetilde{\mathbf{x}}, \kappa_z, \omega; \widetilde{\mathbf{x}}_i)$ represents the integration kernel.

The BEM formulation in the Bézier-Bernstein space employs the Lagrange interpolant relative to the Bernstein basis for the field variable approximation. The field approximation given by the shape function interpolates $(n+1)$ nodal values through the element shape functions ϕ^i of order n, for $i = 0, \dots, n$. Then, the field approximation becomes:

$$a(t) = \sum_{i=0}^{p} \phi^i(t) a^i = \sum_{i=0}^{p} \left\{ \sum_{k=0}^{n} c_k^i B_k^n(t) \right\} a^i = \sum_{i=0}^{p} R^i(t, \dots, t) a^i, \tag{13}$$

where the evaluation of the element shape function $\phi^i(t)$ also benefits from the computational advantages of using the polar form $R^i(t_1, \dots, t_p)$ according to Equation (10).

Once the geometry and the field approximation given by Equations (11) and (13) are introduced into the boundary integral equation of each subdomain, the integrals can be computed using a standard Gauss-Legendre quadrature with $(p+1)$ integration points whenever the collocation point is sufficiently distant from the integration element. Otherwise, the solution of singular or weakly singular integrals is numerically computed using the quadrature rule proposed in References [41].

Then, Equations (2) and (6) are rewritten as follows:

$$\widetilde{\mathbf{H}}_s(\widetilde{\mathbf{x}}, \kappa_z, \omega; \widetilde{\mathbf{x}}_i)\widetilde{\mathbf{u}}(\widetilde{\mathbf{x}}, \kappa_z, \omega) = \widetilde{\mathbf{G}}_s(\widetilde{\mathbf{x}}, \kappa_z, \omega; \widetilde{\mathbf{x}}_i)\widetilde{\mathbf{t}}(\widetilde{\mathbf{x}}, \kappa_z, \omega) \tag{14}$$

$$\widetilde{\mathbf{H}}_f(\widetilde{\mathbf{x}}, \kappa_z, \omega; \widetilde{\mathbf{x}}_i)\widetilde{p}(\widetilde{\mathbf{x}}, \kappa_z, \omega) = \widetilde{\mathbf{G}}_f(\widetilde{\mathbf{x}}, \kappa_z, \omega; \widetilde{\mathbf{x}}_i)\widetilde{v}(\widetilde{\mathbf{x}}, \kappa_z, \omega) \tag{15}$$

where $\widetilde{\mathbf{H}}_s$, $\widetilde{\mathbf{G}}_s$, $\widetilde{\mathbf{H}}_f$ and $\widetilde{\mathbf{G}}_f$ are the fully non-symmetrical boundary element system matrices for solids and acoustic subdomains, respectively.

2.4. Subdomains coupling procedure

Solid subdomains such as rail and rail pads are coupled by imposing equilibrium of forces and compatibility of displacements at solid interfaces. Equilibrium of forces at the interface is fulfilled by integrating nodal tractions according to the element shape function $\mathbf{N} = [\phi_0, \dots, \phi_p]$:

$$\widetilde{\mathbf{f}} = \int_{\Gamma_s} \mathbf{N}^T \widetilde{\mathbf{t}} \mathbf{N} \, d\Gamma = \mathbf{T}\widetilde{\mathbf{t}} \tag{16}$$

Substituting Equation (16) into Equation (14) yields the following:

$$\widetilde{\mathbf{f}} = \mathbf{T}\widetilde{\mathbf{G}}_s^{-1}\widetilde{\mathbf{H}}_s\widetilde{\mathbf{u}} \tag{17}$$

Then the coupled system for solid subdomains is obtained by imposing the equilibrium and compatibility conditions at the interface:

$$\widetilde{\mathbf{K}}_s(\widetilde{\mathbf{x}}, \kappa_z, \omega; \widetilde{\mathbf{x}}_i)\widetilde{\mathbf{u}}(\widetilde{\mathbf{x}}, \kappa_z, \omega) = \widetilde{\mathbf{f}}(\widetilde{\mathbf{x}}, \kappa_z, \omega) \tag{18}$$

The solid and fluid subdomains are assembled next. The coupling of Equations (15) and (18) is carried out by imposition of equilibrium and compatibility conditions of normal pressure and displacement at the interface Γ_{sf} between the track system and the air medium, and null shear stresses. These conditions are fulfilled through the following system of equations [47]:

$$\begin{bmatrix} \widetilde{\mathbf{K}}_s & \mathbf{R}^T \\ -\widetilde{\mathbf{G}}_f\mathbf{N}^T & \widetilde{\mathbf{H}}_f \end{bmatrix} \begin{bmatrix} \widetilde{\mathbf{u}} \\ \widetilde{p} \end{bmatrix} = \begin{bmatrix} \widetilde{\mathbf{f}} \\ 0 \end{bmatrix} \tag{19}$$

where $\mathbf{R}$ is the coupling fluid-solid matrix which relates force and pressure at the interface Γ_{sf}:

$$\widetilde{\mathbf{f}} = -\int_{\Gamma_{sf}} \mathbf{N}^T \mathbf{n} \widetilde{p}\, d\Gamma = \mathbf{R}^T \widetilde{p} \tag{20}$$

where $\mathbf{n}$ is the outward normal vector at Γ_{sf}.

3. Experimental and numerical validation

In this section, the proposed method is validated through comparisons with both experimental data and numerical models. First, the results are compared with those obtained by Zhang et al.[42], which include both experimental data and a numerical model. Then, a separate comparison is made with the method proposed by Knuth et al.[43], providing further validation of the model's performance across different approaches.

3.1. Comparison with experimental test and numerical results

To perform an initial validation of the described method, a comparison is made with an experimental test that was conducted in a semi-anechoic chamber at the Institute of Sound and Vibration Research (ISVR), University of Southampton [42]. The experiment used a 2-meter-long 1:5 scale model of a slab track constructed with reinforced concrete with steel rails. Rubber pads and intermediate steel plates supported the rails. This setup was used to study the effects of noise control treatments, such as absorptive mats and low-height noise barriers, on the noise radiated by the rail vibration.

In this section the proposed method is validated by comparing the numerical results obtained from its application with the experimental data from the test involving the introduction of a noise barrier and a railway vehicle. Additionally, Zhang et al. [42] presented their own numerical results, which were compared with the experimental measurements. These results are further contrasted with those obtained from the model presented in this study.

To carry out a comprehensive study, four numerical models were defined. The first, which serves as the basis for all others, represents a rail on a stepped platform (Figure 2(a)), replicating the experimental test conducted at ISVR. All models, both proposed and reference, include a rigid ground plane beneath the platform. To align with the 2D BEM numerical approach used by Zhang et al.[42], both the simplified rail geometry and the method of modelling the rail pad were adopted from their study, based on the data provided by the authors. Rather than modelling the rail pad as a solid material, it was represented through the combination of results from two different boundary conditions applied at the rail foot base: one with fixed displacements and another with free displacements. The base of the rail foot is positioned 15.0 mm above the platform, representing the thickness of the rail pad. The pressure distributions obtained from the solutions of these two problems were then combined, as outlined in Reference [48].

Once the first model is established as a baseline, three additional models are developed, as shown in Figure 2: (b) one incorporating a noise barrier, (c) another with the inclusion of a railway vehicle, and (d) a third combining both elements.

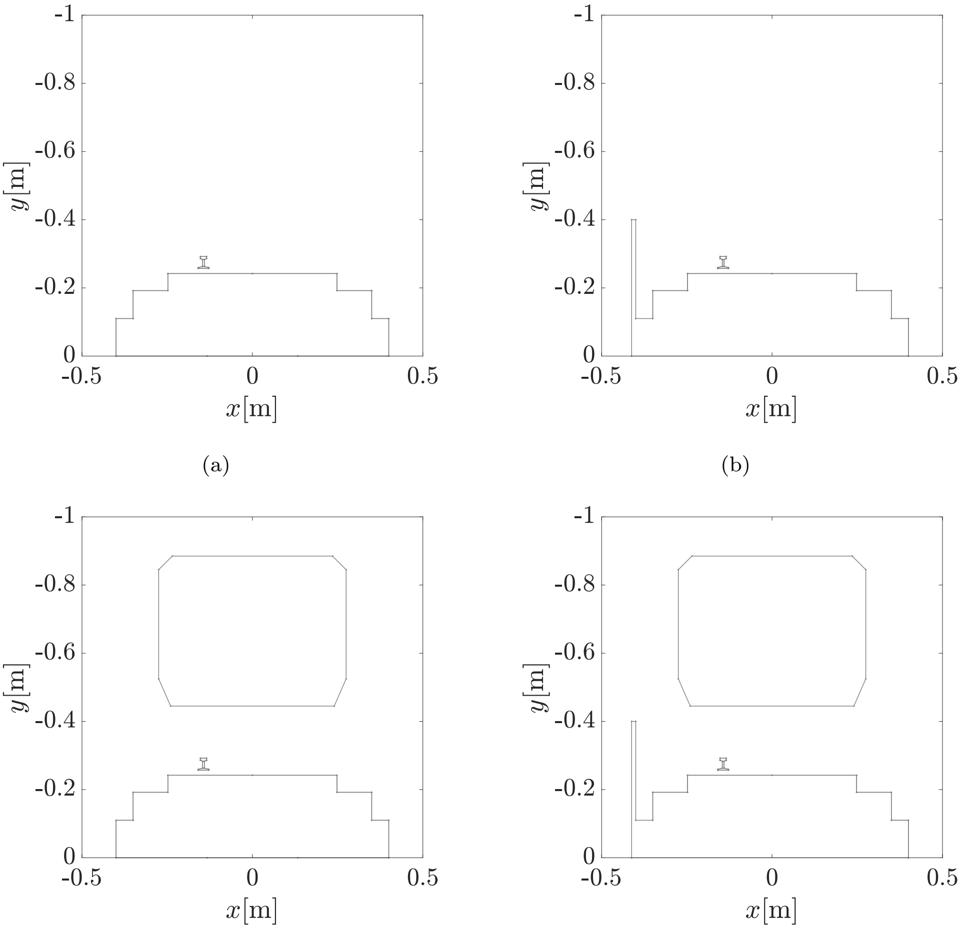

(a)

(b)

(c)

(d)

Figure 2: Models implemented in the considered scenarios: (a) initial platform conditions, (b) with noise barrier, (c) with railway vehicle, and (d) with both noise barrier and railway vehicle.

The rail material used is steel, with a density of $\rho_r = 7850\,\mathrm{kg/m^3}$, a Young's modulus of $E_r = 210\,\mathrm{GPa}$, a Poisson's ratio of $\nu_r = 0.34$, and a rail damping loss factor of $\xi_r = 0.02$. For the air, a density of $\rho_f = 1.225\,\mathrm{kg/m^3}$ and a sound propagation velocity of $c_f = 340\,\mathrm{m/s}$ were assumed. To achieve closer alignment with the approach proposed by Zhang et al. [42], a unit velocity is distributed uniformly over the entire rail boundary. The problem is solved separately for vertical and horizontal velocity conditions to obtain the rail's response in both cases. The boundary conditions for the remaining elements - platform, noise barrier, and railway vehicle - are defined as reflective surfaces, with a zero normal velocity applied. As the models are composed of straight elements due to the simplification of the geometry, the implemented Bézier-Berstein patches[44] are linear. In all the models considered, the boundary is discretised into elements, ensuring that $\kappa_f h = 3$ and a nodal density per wavelength $d_\lambda = (2\pi p)/(\kappa_f h) = 12$, where $\kappa_f = \omega/c_f$, with h and p representing the element length and order, respectively.

Each case was solved over a set of 60 logarithmically spaced frequencies, from 400 to 24000 Hz in the 1:5 scale model, which corresponds to 80 to 4800 Hz in full scale. This range ensures that all one-third-octave bands between central frequencies from 100 to 4000 Hz are fully covered. In scaled mechanical models, dimensions are reduced by the scale factor, while material properties stay the same [42]. This results in natural frequencies being scaled up, with stiffness and mass changing accordingly. To align with full-scale behaviour, frequencies are adjusted downward by the scale factor. For comparison with the model presented by Zhang et al. [42], the problem is treated in 2D, and thus κ_z is assumed to be 0 rad/m.

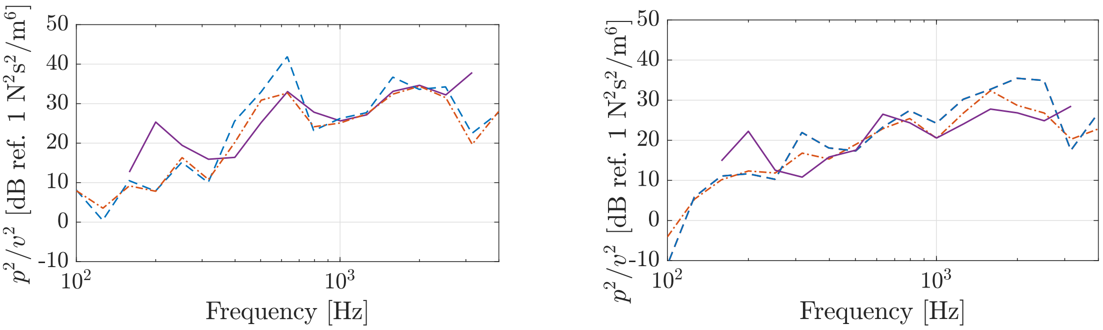

(a)

(b)

Figure 3: Ratio between sound pressure and rail velocity (p^2/v^2) comparison at the evaluation point $(x, y) = (7.5, 1.2)$ m between: proposed model (dashed), experimental data (solid), and numerical results from Ref. [42] (dash-dotted). Results are shown for full-scale frequencies: (a) without barrier, and (b) with barrier.

Figure 3 presents a comparison of the ratio between sound pressure and rail velocity (p^2/v^2), for a system that includes the vehicle, showing results from the proposed method, experimental data, and numerical results from Zhang et al. [42]. Figure 3(a) corresponds to the case without a barrier, while Figure 3(b) illustrates the case with the vertical barrier. The data is presented in one-third octave bands, with the frequencies considered in full scale. The evaluation point corresponds, in full-scale dimensions, to a position located 1.20 m above the top of the rail and 7.50 m horizontally from the track centreline. In general, the results show strong agreement when compared to both the experimental data and the predictions from the alternative numerical model. At low frequencies, both predictions tend to underestimate the measurements. It is important to note that the numerical results are influenced by the exact point at which the calculation is made, exhibiting significant variability over small distances.

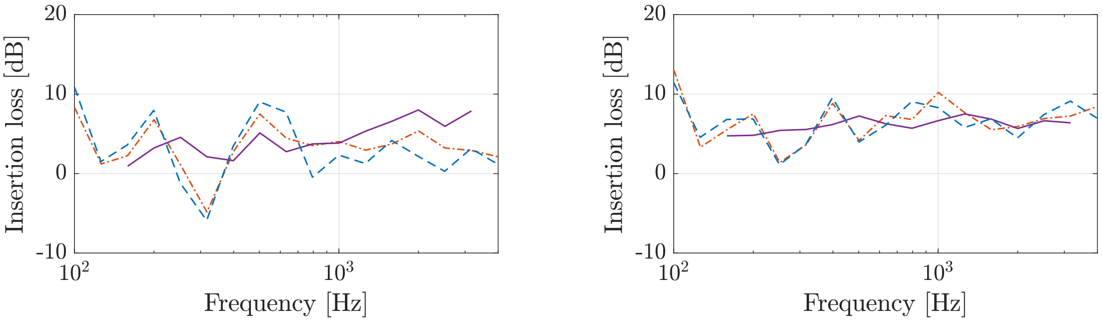

(a)

(b)

Figure 4: Average insertion loss (IL) over four receiver positions at $x = 7.5\,\mathrm{m}$, $y = 0, 1.2, 2.5, 3.5\,\mathrm{m}$, comparing the proposed model (dashed), experimental data (solid), and numerical results from Ref. [42] (dash-dotted). Results are presented for full-scale frequencies: (a) vertical rail vibration, and (b) lateral rail vibration.

Regarding the insertion loss due to the barrier, which is highly sensitive to the domain point, an average is calculated using four receiver positions at $x = 7.5\,\mathrm{m}$ from the track centreline. In full-scale dimensions, these positions correspond to heights of $y = 0, 1.2, 2.5$, and $3.5\,\mathrm{m}$ above the top of the rail. This approach follows the procedure used in the reference article. While some deviation from the experimental results is observed, there is generally a strong agreement between the models, with divergence occurring at higher frequencies. In any case, both numerical and experimental results show that the insertion loss due to the addition of the barrier, considering the presence of the vehicle, averages around 4-5 dB for both vertical and lateral rail vibrations.

After validating the model results, a new calculation is performed considering a larger number of points within the domain, with a fixed full-scale frequency of 1000 Hz (Figure 5). This allows for a more detailed view of the pressure variability and its dependence on the chosen point within the domain. Figures 5(a) and 5(b) present the pressure distribution before and after the introduction of the barrier, respectively, while Figure 5(c) illustrates the attenuation induced by its implementation. A reduction of up to 15 dB is observed behind the barrier. However, this reduction is variable and, in some cases, even amplification is possible due to interference from the different elements considered in the model.

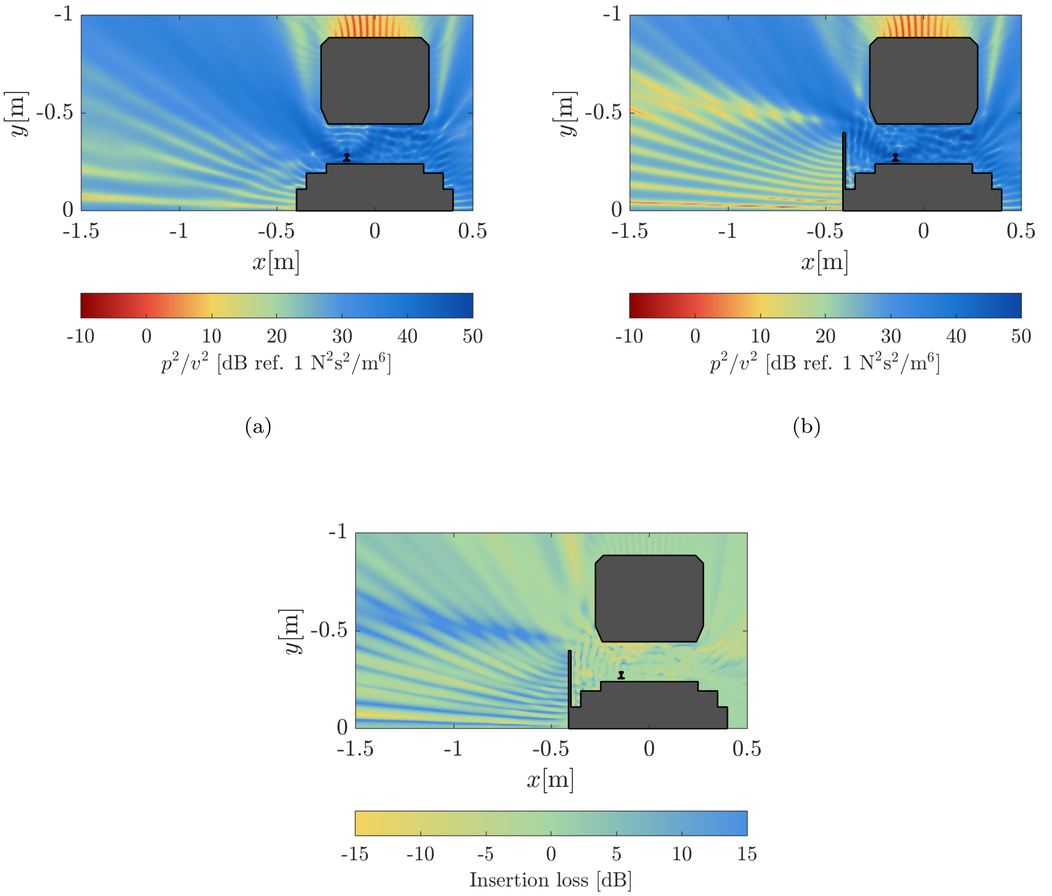

(a)

(b)

(c)

Figure 5: Distribution of the relation between pressure and velocity at 1000 Hz: (a) before and (b) after barrier implementation, and (c) insertion losses.

3.2. Comparison with a 2.5D FEM-BEM model

Finally, the model is further validated through a comparative analysis with the methodology proposed by Knuth et al.[43], which employs a 2.5D Finite Element Method (FEM) for the structural track model coupled with a 2.5D Boundary Element Method (BEM) for the acoustic domain. The comparison considers a UIC60 rail continuously supported on a rail pad and subjected to a unit vertical point load applied at the center of the railhead (Figure 6).

It is important to highlight some differences between the two approaches. In Knuth et al.'s 2.5D FEM method [43] a semi-analytical formulation can be used to calculate the vibration directly in the spatial or wavenumber domain. This is different from the proposed model, where the spatial solution ($\mathbf{a}(\mathbf{x}, \omega)$) is obtained from the wavenumber solution ($\mathbf{a}(\widetilde{\mathbf{x}}, \kappa_z, \omega)$) (see Eq. (1)). Additionally, Knuth et al.'s formulation [43] assumes one-way coupling only, in comparison with the proposed approach, see Eq.(19), where the influence of the sound field on the vibration is captured. Despite these differences, the 2.5D FEM method provides a benchmark for evaluating the frequency response of the rail.

	Rail	**Rail pad 1**
Young's modulus [MPa]	210×10^3	3.2
Density [kg/m^3]	7860	10
Poisson's ratio [-]	0.3	0.45
Damping loss factor [-]	0.02	0.25

Table 1: Material properties for the validation model.

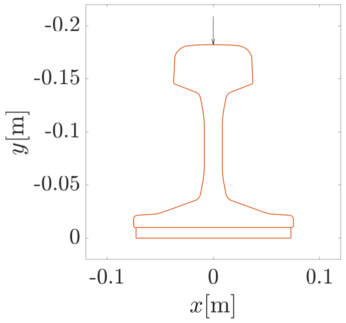

Figure 6: Model geometry and load application point for the analysed track system.

The 2.5D analysis is conducted for 300 frequencies logarithmically spaced between 10 and 5000 Hz. The number and values of wavenumbers (κ_z) selected for integration are individually adapted at each frequency to optimize the computation of the system's response, increasing the density of points close to wavenumbers at which the response reaches a peak and reducing it in flatter regions to improve computational efficiency.

The track system consists of a UIC60 rail profile placed on a 10 mm-thick rail pad. It is exposed to air along its entire boundary, except for the bottom of the rail pad, which is attached to a rigid surface at $y = 0$. To represent the rail system and the surrounding air medium, three subdomains are defined. The material properties used in the validation model are summarised in Table 1, while the air properties are the same as those in the experimental comparison in Section 3.1.

The boundary of the rail is represented by 36 cubic Bézier patches, while the rail pad is implemented using 4 linear Bézier patches. This modeling approach ensures matching nodes on the contact surface between the rail and the rail pad, facilitating their coupling. Moreover, the fluid interface over the rail system is represented using 37 cubic Bézier patches, aligning with the outer boundary of the solid domain and coinciding with each patch of it. The fluid domain patch corresponding to the base of the rail pad does not exist, as this area is not in contact with the fluid. Thus, the system is subjected to zero-displacement boundary conditions at the ground. For the consideration of the ground as a rigid reflective surface, the method of images [49] has been used through the application of Green's functions in the half-space. A unit vertical point load is applied at the central node of the railhead, allowing for the comparisons presented below.

The first comparison focuses on the point mobility of the rail at the load application point. This mobility is defined as the velocity at $z = 0$ divided by the total applied force, which in this case has unit amplitude. A half-cosine force distribution with an excitation length of $\beta = 9.4\,\mathrm{mm}$ along the z-direction is assumed, as explained in [50], to avoid a singularity for the case of a point load at high frequencies, which arise from the increasing number of waves excited when applying a constant force at $z = 0$. Figure 7(a) compares the point mobility results for both models. A good agreement is observed, with the results closely matching, except for slight discrepancies at higher frequencies. The transfer mobility at $z = 2.5\,\mathrm{m}$ is also compared in Figure 7(b). The results show more deviation at frequencies below the rail-on-pad resonance around 270 Hz, where the rail vibration mainly consists of rapidly decaying near-fields, but still exhibit good overall agreement. At higher frequencies, the differences are reduced, as these values are not obtained at the load application point and are therefore less affected by the higher-order waves.

The results for sound power and radiation efficiency, as defined in [50], are also compared in Figures 7(c) and 7(d). The agreement between the models is generally good, with only minor differences in the computed results. Additionally, sound pressure levels within the domain have been compared at three points, located at vertical distances of 1.20 m from the railhead, at lateral distances $x = 0\,\mathrm{m}$, $x = 1.5\,\mathrm{m}$, and $x = 3.0\,\mathrm{m}$ on the planes $z = 0\,\mathrm{m}$ and $z = 2.5\,\mathrm{m}$. Figure 8 shows the results for these points, where a good overall agreement is observed.

In general, the results obtained with the proposed model show good agreement with those of Knuth et al.[43], with only minor discrepancies noted. The model demonstrates reliable performance, yielding results that closely match the reference data across various aspects, thereby confirming its reliability and

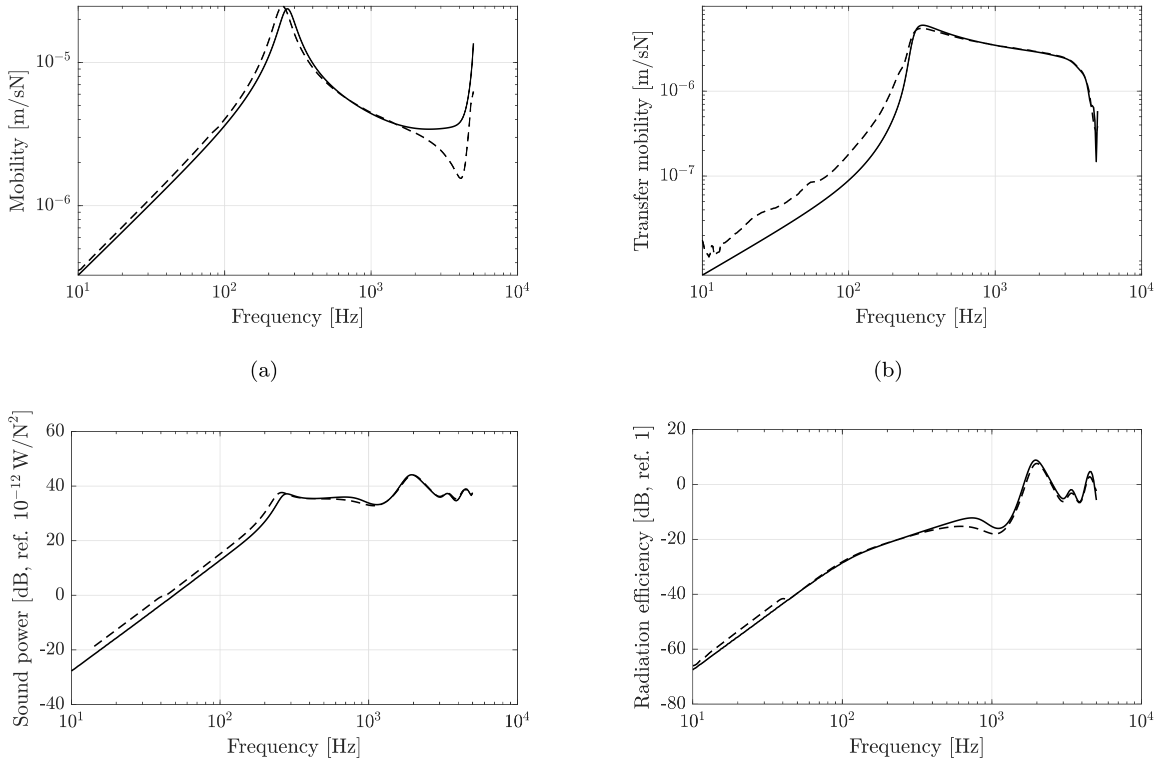

(a) (b)

(c) (d)

Figure 7: Knuth et al. [43] model (solid) and the proposed model (dashed) results: (a) point mobility, (b) transfer mobility at $z = 2.5\,\mathrm{m}$, (c) sound power for a unit force and (d) radiation efficiency.

consistency. In terms of computational efficiency, the numerical workflows and coding strategies of both methods differ significantly, making a direct comparison between the two implementations challenging and unlikely to yield representative or conclusive results.

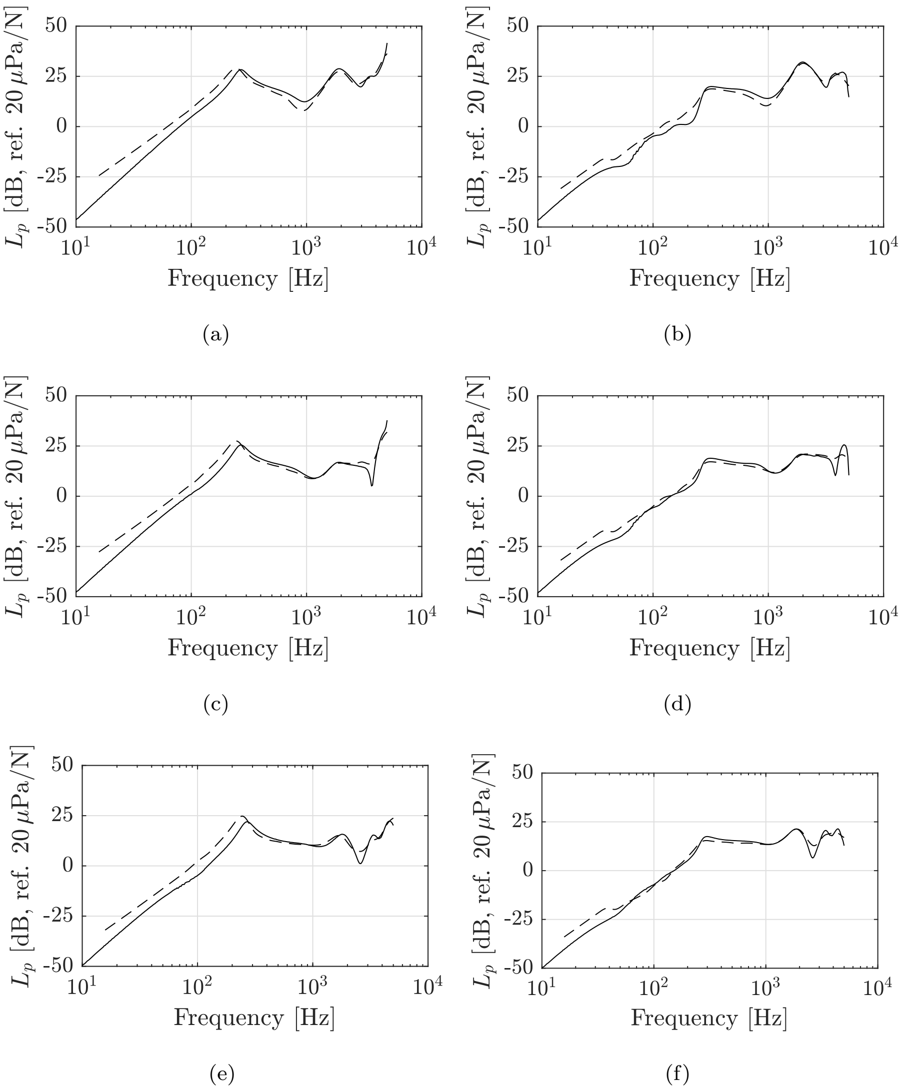

(a)

(b)

(c)

(d)

(e)

(f)

Figure 8: Sound pressure level at 1.2 m above the railhead with (a,c,e) $z = 0$ m and (b,d,f) $z = 2.5$ m. (a,b) correspond to $x = 0$ m, (c,d) to $x = 1.5$ m, (e,f) to $x = 3.0$ m for the (solid) Knuth et al.[43] model and the (dashed) proposed model.

4. Track systems comparison

In this section, the proposed method is applied to analyse the behavior of three different track systems under a vertical point load at the center of the railhead (Figures 6 and 9), aiming to compare their performance. The approach follows the same methodology as described in the previous section for the numerical model validation, with cases calculated in two and a half dimensions due to their longitudinal invariance. The analysis is conducted over a frequency range of 10 to 5000 Hz, using 300 logarithmically spaced points within this range. As in the previous comparison, the number and values of wavenumbers (κ_z) selected for integration are individually adapted at each frequency to optimize the system's response computation. This approach increases the density of points around peaks in the response and reduces it in flatter regions, thereby improving computational efficiency.

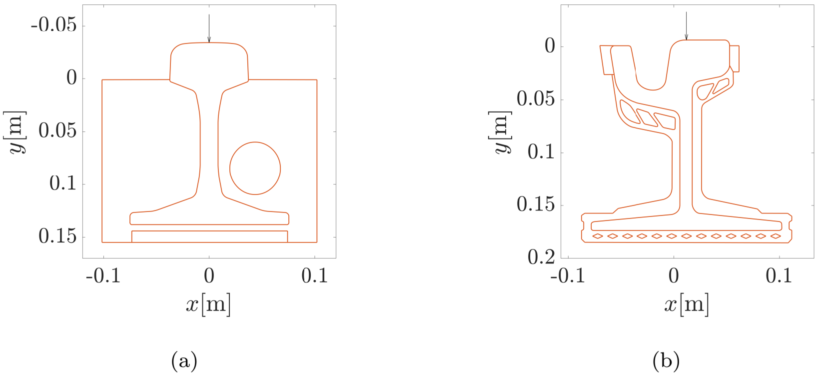

(a)

(b)

Figure 9: Model geometry and load application point on the (a) UIC60 embedded system and (b) 60R1 grooved rail embedded system.

The first rail system under study is a UIC60 rail profile, installed on a 10 mm high rail pad. The model considered is the same as the one previously defined for comparison with the numerical model by Knuth et al.[43] (Figure 6), but with updated material properties, as presented in Table 2, to make the rail pad stiffer and comparable to the other models. The geometry of the system, the boundary conditions, and the applied load all remain the same as those used in the validation example.

The next rail system analysed is an Embedded Rail System (ERS) composed of a UIC60 rail profile, an elastomeric material, and an under-rail pad, all embedded within a surrounding medium (Figure 9(a)). In this case, the track cross-section is divided into three subdomains representing the structural components of the track, with an additional domain for the surrounding air. The material properties of these components are provided in Table 2. The boundaries of the rail, elastomeric material, and under-rail pad are implemented using cubic Bézier patches [44] to ensure continuity and smooth coupling across the interfaces. Specifically, 36 patches are used for the rail, 42 for the elastomeric material, and 4 for the under-rail pad. For the fluid

	Rail	**UIC60 systems: on a pad and embedded**		**60R1 embedded**	
		Rail Pad 2	**Elastomeric material**	**Positioners**	**Elastomeric material**
Young's modulus [MPa]	210×10^3	15	20	15	50
Density [kg/m^3]	7860	1000	1500	1000	1100
Poisson's ratio [-]	0.3	0.45	0.35	0.45	0.45
Damping loss factor [-]	0.01	0.25	0.25	0.25	0.25

Table 2: Material properties of the rail and components used in each configuration.

domain, 9 patches are used, as the track system is embedded, leaving only the upper boundary, comprising the railhead and the exposed surface of the elastomer, in contact with the air. The boundary conditions within the elastomeric void are defined by zero stress, and the ground is treated as a rigid surface at $y = 0\,\mathrm{m}$.

Finally, the same analysis is applied to a more complex track system, consisting of an embedded 60R1 rail within an elastomeric material with voids, along with two lateral positioners (Figure 9(b)). The material properties used for this model are summarised in Table 2. For each of the system's elements, a separate domain has been defined, resulting in a total of four subdomains composing the cross-section. Specifically, 31 patches were required to define the rail. Due to the presence of numerous voids, the elastomeric material required 146 patches to achieve an accurate geometric representation. The lateral positioners were defined using 5 and 6 patches, respectively. All solids are coupled to each other and the fluid, represented by 10 patches. As the system is embedded, the fluid domain only interacts with the upper surface of the rail and lateral positioners, which are exposed to the air. The boundary conditions for the elastomer's voids are also characterised by zero stresses, while zero displacements have been prescribed to the outer surface of the elastomer. As in the previous cases, the surrounding ground surface is modeled as a rigid reflective boundary at $y = 0.05\,\mathrm{m}$, which enables realistic interaction conditions for the embedded rail configuration, while maintaining the fluid domain in the negative y-plane.

In all the models described, the discretisation of the entire boundary into elements is conducted, ensuring that $\kappa_f h = 3$ and a nodal density per wavelength $d_\lambda = \frac{2\pi p}{\kappa_f h} = 12$.

A comparative analysis is then performed to evaluate the responses of the different models under a vertical point load applied at the central point of each railhead. For the 60R1 grooved rail, this corresponds to the central region where the wheel makes contact as shown in Figure 9(b).

4.1. Point mobility

Figure 10 shows the magnitude and phase of the vertical point mobility of the rail at the load application point for each track system. As in the previous section, a half-cosine distributed force is applied along the z-

direction, with an excitation length of $\beta = 9.4\,\mathrm{mm}$, following the approach described in [50]. The behaviour of each type of track is strongly influenced by the stiffness of the support systems, as the rail support stiffness can vary across a wide range, thereby significantly impacting the track's dynamic performance.

At low frequencies, the embedded UIC60 track system exhibits higher mobility, whereas the 60R1 grooved track system shows the lowest one. This behavior is primarily attributed to differences in overall support stiffness, which are reflected in the frequency shift of the maximum resonance peak for each track type. Notably, the embedded UIC60 system presents a secondary peak corresponding to torsional vibrations of the rail, induced by the asymmetry of the support material. The prominent peaks in the system's response result from the resonance of the rail mass on the stiffness of its support. Below this frequency, the mobility is primarily dictated by the support's stiffness, while at higher frequencies, it is predominantly influenced by the rail's bending stiffness.

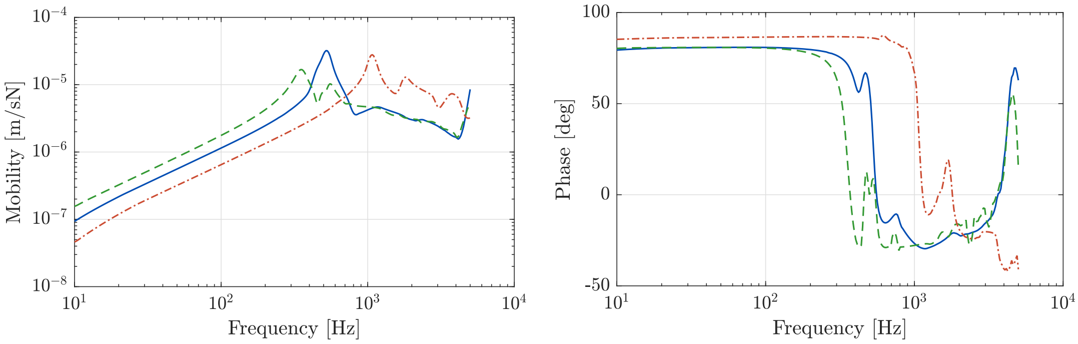

(a)

(b)

Figure 10: Point mobilities (a) magnitude and (b) phase of the different rail configurations: UIC60 railpad system (solid), UIC60 embedded system (dashed) and 60R1 grooved rail embedded system (dash-dotted).

4.2. Wave dispersion

Figure 11 illustrates the dispersion relations in terms of velocity resulting from vertical excitation for the track systems under analysis. A similar behaviour can be observed across all three types of track systems, with the bending wave clearly dominant.

Figures 12, 13, and 14 show the deformed shapes of the three track systems at selected frequency-wavenumber combinations, corresponding to prominent peaks in the dispersion curves presented in Figure 11. Figure 12 refers to the rail-on-rail pad system, with the main peak corresponding to vertical bending waves. In the case of the embedded UIC60 system, the deformation primarily develops within the embedding layer, due to its lower stiffness. The deformed shapes illustrated in Figure 13 correspond to (a) vertical bending waves and (b) torsional waves. Finally, Figure 14 presents the deformation corresponding to the embedded grooved rail system. In this case, the system's complexity leads to a more complicated response.

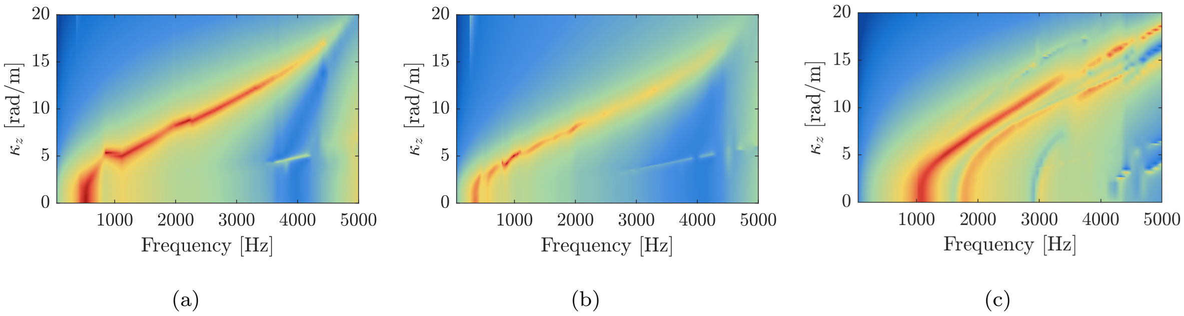

Figure 11: Dispersion relations in terms of rail velocity for (a) the UIC60 rail over a pad, (b) the UIC60 embedded track system and (c) 60R1 grooved rail embedded system.

Nevertheless, Figure 14(a) still reveals a vertical displacement associated with bending wave propagation, whereas Figure 14(b) shows a combination of rail torsion and vertical displacement.

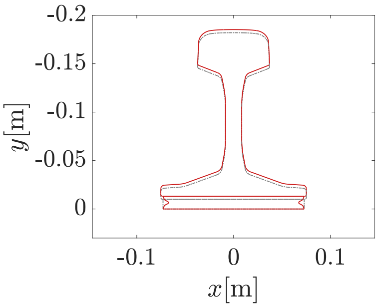

Figure 12: Deformed shapes of the UIC60 on a rail pad system at (a) 529 Hz with $\kappa_z = 0$ rad/m.

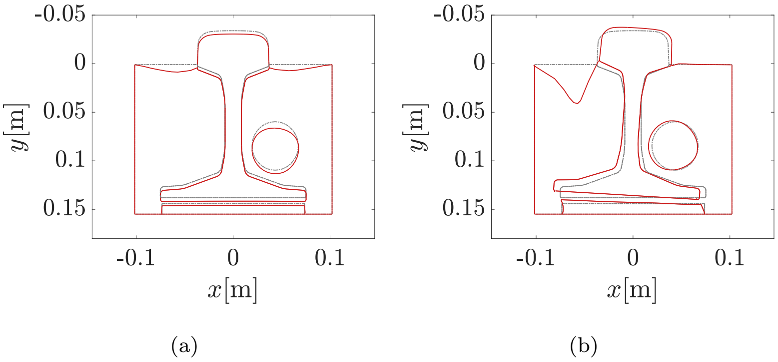

Figure 13: Deformed shapes of the UIC60 embedded system at (a) 356 Hz with $\kappa_z = 0\,\text{rad/m}$ and (b) 552 Hz with $\kappa_z = 3\,\text{rad/m}$.

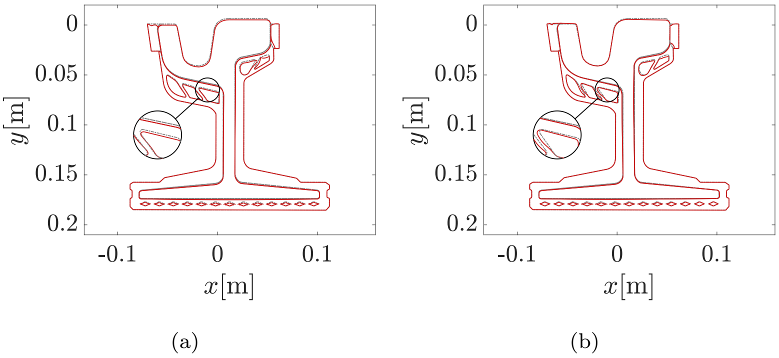

Figure 14: Deformed shape of the 60R1 grooved rail embedded system at (a) 1074 Hz and (b) 1882 Hz with $\kappa_z = 0\,\text{rad/m}$.

4.3. Radiated power

In Figure 15, the sound power of each track system is shown. The embedded UIC60 system exhibits higher sound power levels at lower frequencies, which is due to the vibration of the upper surface of the embedding material. Its lower stiffness results in greater deformation of the embedding material under rail excitation, leading to higher radiated sound power. In contrast, the grooved rail configuration exposes only a small portion of the embedding material to the air, and the vibration of this surface is less pronounced. In all cases, a behaviour consistent with the results presented in Subsection 3.2 can be observed, with a distinct peak occurring near the resonance frequency. The grooved rail configuration exhibits a distribution broadly consistent with that reported in [51], despite differences in the embedding material properties.

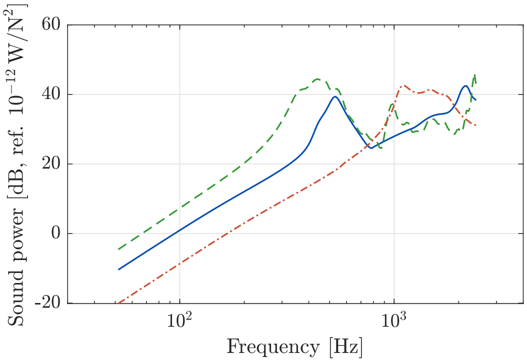

Figure 15: Sound power of the different rail configurations for a unit force: UIC60 rail pad system (solid), UIC60 embedded system (dashed) and 60R1 grooved rail embedded system (dash-dotted).

5. Noise barriers

After comparing the different track systems, this section examines the effectiveness of barriers in mitigating radiated noise. For this analysis, a UIC60 rail on a railpad is used, maintaining the same material properties described in Table 2, and subjected to a unit vertical point load applied at the center of the railhead. The aim is to evaluate the impact of barrier insertion, as well as the influence of the vehicle's presence, on radiated noise from the rail. To simplify the analysis and avoid the artificial interference that would arise from considering both rails, only a single rail is modeled, which is representative and sufficient to capture the essential characteristics of the problem. To this end, six additional models are developed for comparative analysis, building upon the reference model previously described.

The reference model consists of the track system without any mitigation measure, providing a baseline for comparison. The first new model introduces a straight, tall barrier located at 4 m from the center of the outer rail, while the second model considers the same barrier positioned closer, at 2.5 m. The third model instead considers a low-height curved barrier located at 1.70 m from the track axis (0.98 m from the center of the analysed rail). The fourth model builds upon this low-height curved barrier by including a simplified S-103 vehicle [52], allowing assessment of its effect on radiated noise. The fifth model consists of a low-height straight barrier including the vehicle, designed to assess the influence of the upper curvature on the encapsulation effect. Finally, the sixth model considers a low-height barrier similar to the curved barrier, but with the upper part replaced by a single straight segment inclined at 40° from the vertical, also including the vehicle. This configuration allows comparison of an alternative low-height barrier geometry. In each case, the necessary patches were added to the fluid domain of the model to properly define the barrier or vehicle boundaries.

The straight barrier, with a height of 3 m and a thickness of 0.05 m, is used in two separate models: one with the barrier positioned at 4.0 m (first model) and another with it at 2.5 m (second model) from the outer rail. Four linear patches are used to model the barrier in each case, with boundary conditions set to zero normal velocity for all of them. As a result, the barrier acts as a fully reflective surface, reflecting the waves generated by the rail vibration and amplifying wave propagation in the region between the rail and the barrier.

The low-height curved barrier (third model) is defined using six patches. It has a curved shape (Figure 16(a)) in the upper part designed to encapsulate the radiated noise, directing it toward the ground and thus reducing noise transmission behind it. Similar to the straight barrier, the low-height barrier also has reflective boundary conditions, causing the acoustic waves to be redirected rather than dissipated.

In the fourth model, the low-height curved barrier is combined with a simplified S-103 vehicle [52]. The geometry of the vehicle is positioned such that the distance from its lower patch to the railhead is 0.92 m, corresponding to the wheel diameter. This implementation requires a total of 33 cubic patches to accurately

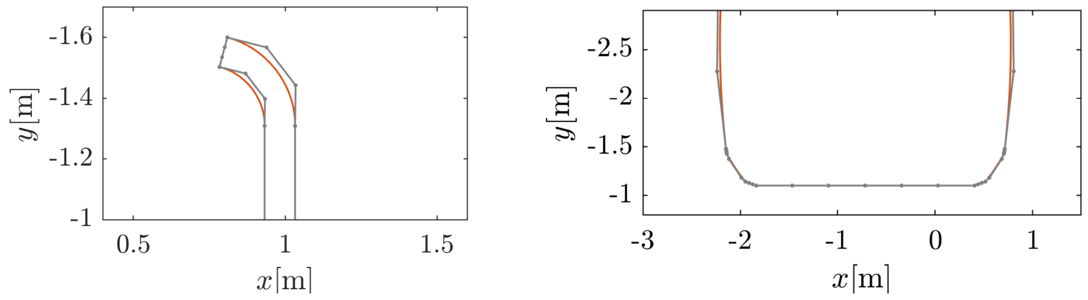

(a)

(b)

Figure 16: Zoom of the geometry for (a) the low-height curved barrier and (b) the S-103 vehicle.

define the vehicle's boundary. Figure 16(b) illustrates the lower part of the geometry of the vehicle and the control points required for its implementation. The purpose of this model is to analyse the vehicle's effect on sound encapsulation, providing a more realistic approximation of the railway system. However, since the surface is still considered reflective, the absorption properties of the vehicle material (or the ground) are not accounted for, simplifying the model by neglecting its potential noise attenuation.

To further investigate the encapsulation effect in the presence of the vehicle and the influence of barrier geometry, two additional models were developed. In both cases, the vehicle is defined as in the fourth model, and the barriers are positioned at the same location as the low-height curved barrier. The fifth model features a low-height straight barrier of the same total height as the curved barrier, represented with four linear patches, while the sixth model consists of a low-height barrier similar to the curved barrier but with the upper part replaced by a single straight segment inclined at 40° from the vertical, giving a geometry represented by six linear patches. Reflective boundary conditions are applied to both the barrier and the vehicle, allowing the influence of barrier geometry on wave propagation to be directly observed.

Figure 17 presents the real part of the sound pressure for four representative models at a frequency of 1400 Hz and $\kappa_z = 0\,\mathrm{rad/m}$, enabling a direct comparison. The selected cases comprise the configuration without a barrier, the tall straight barrier at $x = 4, \mathrm{m}$, and the low-height curved barrier both without and with the vehicle. These configurations capture the characteristic behaviour associated with each barrier type. For the tall barrier, a reduction in sound pressure levels is observed behind the barrier, accompanied by an increase due to reflected waves in the region between the rail and the barrier. For the low-height curved barrier, the reduction behind the barrier is more pronounced, while the presence of the vehicle highlights the encapsulation effect. This wave reflection, combined with the reflective boundary condition of the track, generates additional reflections, which eventually escape through the gap between the vehicle and the barrier. Consequently, the resulting acoustic field exhibits a more complex distribution, with increased sound pressure in certain regions. The additional models not depicted in this figure, namely the tall barrier

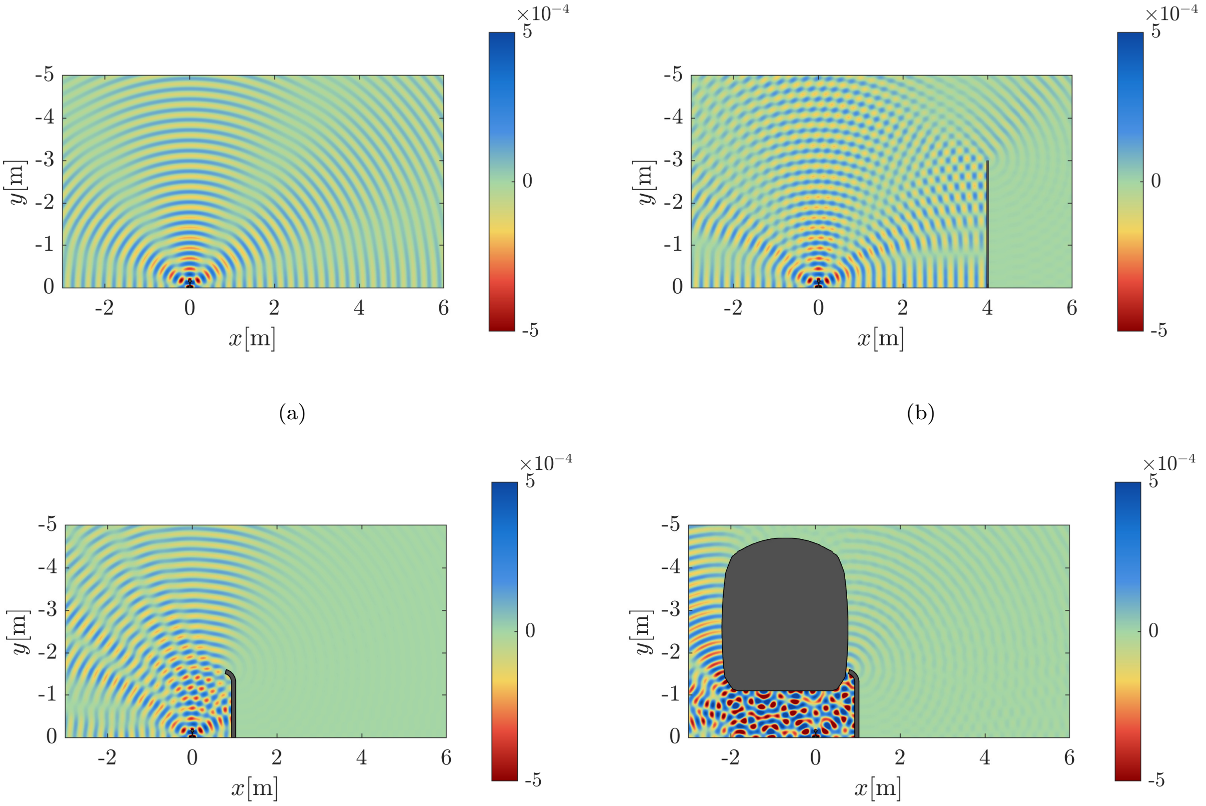

(a)

(b)

(c)

(d)

Figure 17: Real part of the sound pressure [Pa] at 1400 Hz: (a) under initial conditions, (b) with the implementation of a straight reflecting barrier, (c) with a low-height curved reflecting barrier, and (d) with a low-height curved reflecting barrier and an S-103 vehicle.

at $x = 2.5,$m and the low-height barriers with alternative geometries, exhibit qualitatively similar trends, with variations primarily arising from barrier proximity or geometric differences.

To extend the previous comparison, an analysis was conducted by considering various points along the positive x-direction, at a height of 1.20 m above the railhead (with $z = 0$ m) considering all the defined models. This analysis, illustrated in Figures 18(a) and 18(b), evaluates the sound pressure levels as a function of frequency at two specific distances: 2.0 m and 6.75 m from the rail axis, considering the full 2.5D solution.

At $x = 2.0$ m, the observation point lies between the rail and the tall barriers. As a result, no attenuation is achieved; instead, due to the fully reflective boundary condition of the barriers, an amplification of the sound pressure occurs at certain frequencies. This effect is particularly pronounced for the barrier located at $x = 2.5$ m, where the proximity of the reflective surface intensifies the re-radiated waves, while for the barrier at $x = 4.0$ m the effect is less marked. For the low-height barriers, a similar behaviour is observed across the different configurations at this location. When the vehicle is included, the encapsulation effect introduces additional reflections which, combined with those from the barrier, lead to higher sound pressure levels at this observation point. In contrast, for the low-height curved barrier without the vehicle, the sound pressure remains lower, even at higher frequencies. This behaviour is linked to the shorter wavelengths, which can more easily pass through the gap between the vehicle and the barrier, thereby limiting the overall attenuation capacity. At $x = 6.75\,\mathrm{m}$, located behind all the barriers, the tall configurations show clear attenuation, with reductions in sound pressure comparable to those of the low-height curved barrier when the vehicle is not included. When the vehicle is present, the sound pressure level at this point is higher due to additional reflections from the encapsulation effect. As frequency increases, the gradual decrease in attenuation occurs for the same reasons discussed previously.

The effect of the low-height barriers is better illustrated in the insertion losses shown in Figures 18(c) and 18(d). At $x = 2,\mathrm{m}$ and low frequencies, the most effective configurations are those with the upper section inclined towards the vehicle, which encapsulate the noise, whereas the straight low-height barrier exhibits slightly lower insertion losses. At higher frequencies, as the wavelength decreases, the gap between the vehicle and the barrier allows waves to pass, resulting in higher insertion losses for the configuration without the vehicle. In all vehicle-including cases, the insertion losses fluctuate with frequency. At $x = 6.75,\mathrm{m}$, located behind the barriers, the tall configurations generally yield greater insertion losses, particularly at higher frequencies, with values comparable to those of the low-height barrier without the vehicle. The low-height barriers with the vehicle exhibit a behaviour similar to that observed at the previous observation point. A more realistic assessment would require a parametric study at multiple distances and the consideration of the absorptive properties of the materials and the ballast.

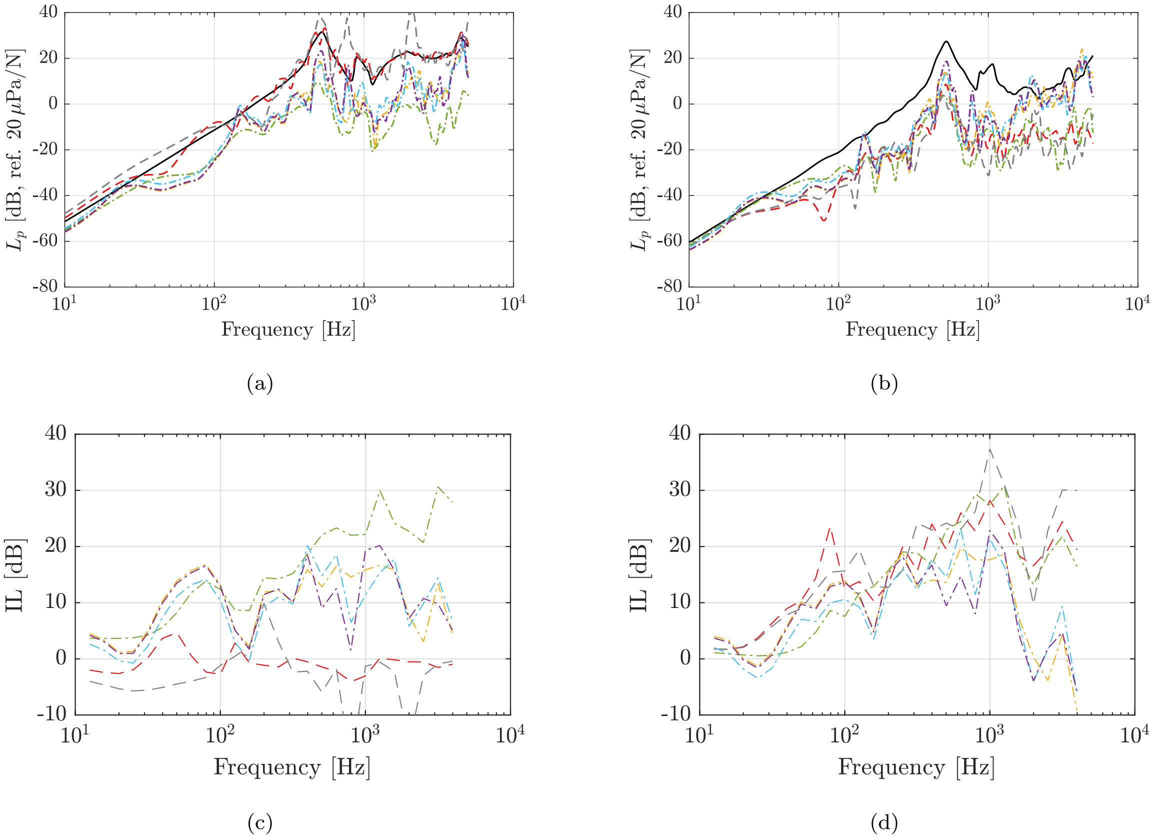

Figure 18: (a,b) Sound pressure levels (L_p) and (c,d) acoustic insertion losses (IL) at 1.20 m above the railhead under different conditions: (solid black) no barrier, (dashed) tall straight barriers at (grey) $x = 2.5$ m and (red) $x = 4.0$ m, (dash-dotted) low-height barriers: (green) curved, and including S-103 vehicle: (yellow) curved, (purple) two-segment inclined, and (blue) straight. Results correspond to (a,c) $x = 2$ m and (b,d) $x = 6.75$ m.

6. Conclusions

A numerical model is presented based on a 2.5D Boundary Element Method (BEM) formulated in the Bézier-Bernstein space to predict vibration and radiated noise from railway systems. The 2.5D formulation computes the 3D solution in the wavenumber-frequency domain, assuming invariance of the problem along the longitudinal direction z and linear elastic behaviour. Unlike most existing methods that employ a coupled FEM-BEM formulation, the proposed approach consistently applies BEM to both the track system and the surrounding acoustic domains. This enables meshing only the boundary of the track system. Moreover, the method enables an exact representation of the track geometry using Bézier-Bernstein basis functions, a technique commonly employed in CAD models. Consequently, it can effectively address problems involving complex geometries that are typically not well captured by standard FEM and BEM formulations. Radiated noise is calculated from the normal displacements on the track surface according to the integral representation of sound pressure. Furthermore, the application of the QUEEN quadrature rule [41] facilitates efficient and accurate numerical integration of the boundary integral equations. This approach supports arbitrary high-order elements, thereby improving both computational efficiency and accuracy, particularly in predicting high-frequency noise.

The model is validated using both experimental results and numerical data from other authors [42, 43], showing generally good agreement with experimental data and other numerical models. In this study, three types of track systems are analysed: rail-on-slab configurations and two embedded rail designs. A comparative analysis is conducted to assess their acoustic performance. The results show that embedded systems radiate less noise at high frequencies; however, at lower frequencies, noise levels can increase depending on the design and materials used in the track system.

Additionally, this methodology enables the incorporation of mitigation measures, such as noise barriers, to assess their effectiveness in reducing noise emissions generated by railway systems. By modelling various barrier geometries, the approach provides detailed insights into how variations in shape, size, and position influence acoustic performance. Furthermore, by incorporating the railway vehicle in the case of low barriers, it is possible to observe the noise encapsulation capabilities of the barrier, highlighting its impact on noise reduction.

CRediT authorship contribution statement

R. Velázquez-Mata: Conceptualization, Methodology, Software, Investigation, Validation, Writing - original draft, Writing - review & editing. C. Knuth: Conceptualization, Methodology, Software, Investigation, Supervision, Writing - review & editing. A. Romero: Conceptualization, Methodology, Software, Investigation, Validation, Funding acquisition, Supervision, Writing - original draft, Writing - review & editing. G.

Squicciarini: Conceptualization, Methodology, Supervision, Writing - review & editing. A. Tadeu: Conceptualization, Methodology, Writing - review & editing. D. J. Thompson: Conceptualization, Methodology, Supervision, Writing - review & editing. P. Galvín: Conceptualization, Methodology, Software, Investigation, Validation, Funding acquisition, Supervision, Writing - original draft, Writing - review & editing.

Declaration of Competing Interest

The authors declare that they have no known competing financial interests or personal relationships that could have appeared to influence the work reported in this paper.

Declaration of Generative AI and AI-assisted technologies in the writing process

During the preparation of this work, AI tools were used to improve the readability and language of the paper. After using this tool/service, the authors reviewed and edited the content as needed and take full responsibility for the content of the publication.

Acknowledgments

The authors would like to acknowledge the financial support provided by the research projects PID2019-109622RB-C21 and PID2022-138674OB-C21 funded by the Spanish Ministry of Science, Innovation and Universities, the Foundation for Science and Technology (FCT) through the project UID/6438/2025 of the research unit CERIS, and the Andalusian Scientific Computing Centre (CICA).

References

[1] EU Directive. Directive 2002/49/EC of the European Parliament and the Council of 25 June 2002 relating to the assessment and management of environmental noise; 2002.

[2] He Y, Thompson D, Hu Z. Aerodynamic noise from a high-speed train bogie with complex geometry under a leading car. Journal of Wind Engineering and Industrial Aerodynamics. 2024;244:105617. Available from: `https://www.sciencedirect.com/science/article/pii/S0167610523003197`.

[3] Castellini F, Faccini L, Di Gialleonardo E, Alfi S, Corradi R, Squicciarini G, et al. Curve squeal in sharp curves: effect of multiple wheel/rail contact points. Applied Acoustics. 2024;218:109862. Available from: `https://www.sciencedirect.com/science/article/pii/S0003682X24000136`.

[4] Torstensson PT, Squicciarini G, Krüger M, Pålsson BA, Nielsen JCO, Thompson DJ. Wheel–rail impact loads and noise generated at railway crossings – Influence of vehicle speed and crossing dip angle. Journal of Sound and Vibration. 2019;456:119-36. Available from: `https://www.sciencedirect.com/science/article/pii/S0022460X19302536`.

[5] Thompson D. Railway noise and vibration. Mechanisms, Modelling and Means of Control. Second edition. London: Elsevier; 2024.

[6] Thompson DJ, Hemsworth B, Vincent N. Experimental Validation of the TWINS Prediction Program for Rolling Noise, Part 1: Description of the Model and Method. Journal of Sound and Vibration. 1996;193(1):123-35. Available from: `https://www.sciencedirect.com/science/article/pii/S0022460X96902527`.

[7] Thompson D, Zhao D, Squicciarini G, Toward M, Cierco E, Jansen E, et al. Methods for separating the noise produced by the wheels and track during a train pass-by. Railway Engineering Science. 2024 10.

[8] European Committee for Standardization. EN 1793-4:2015. Road traffic noise reducing devices - Test method for determining the acoustic performance - Part 4: Intrinsic characteristics. In situ values of sound diffraction. Brussels, Belgium; 2015.

[9] European Committee for Standardization. EN 1793-5:2016. Road traffic noise reducing devices - Test method for determining the acoustic performance - Part 5: Intrinsic characteristics. In situ values of sound reflection under direct sound field conditions. Brussels, Belgium; 2016.

[10] European Committee for Standardization. EN 1793-6:2018+A1:2021. Road traffic noise reducing devices: Test method for determining the acoustic performance - Part 6: Intrinsic characteristics - In situ values of airborne sound insulation under direct sound field conditions. Brussels, Belgium; 2021.

[11] International Organization for Standardization. ISO 10847:1997. Acoustics: In situ determination of insertion loss of outdoor noise barriers of all types. Geneva, Switzerland; 1997.

[12] American National Standards Institute/Acoustical Society of America. ANSI/ASA S12.8-1998 (R2013). Methods for determination of insertion loss of outdoor noise barriers. Melville, New York; 2013.

[13] Federal Highway Administration US Department of Transportation. Highway Noise Barrier Design Handbook. Washington, DC; 2000.

[14] Federal Highway Administration US Department of Transportation. Noise Measurement Handbook. Final Report. Washington, DC; 2018.

[15] Martinez-Orozco JM, Barba A. Determination of Insertion Loss of noise barriers in Spanish roads. Applied Acoustics. 2022;186:108435. Available from: `https://www.sciencedirect.com/science/article/pii/S0003682X21005296`.

[16] Rathe EJ. Note on two common problems of sound propagation. Journal of Sound and Vibration. 1969;10(3):472-9. Available from: `https://www.sciencedirect.com/science/article/pii/0022460X69902259`.

[17] Kurze UJ, Anderson GS. Sound attenuation by barriers. Applied Acoustics. 1971;4(1):35-53. Available from: `https://www.sciencedirect.com/science/article/pii/0003682X71900247`.

[18] Makarewicz R, Jarzęcki J, Berezowska-Apolinarska K, Preis A. Rail transportation noise with and without a barrier. Applied Acoustics. 1989;26(2):135-47. Available from: `https://www.sciencedirect.com/science/article/pii/0003682X89900674`.

[19] Micheli GJL, Farné S. Urban railway traffic noise: Looking for the minimum cost for the whole community. Applied Acoustics. 2016;113:121-31. Available from: `https://www.sciencedirect.com/science/article/pii/S0003682X1630175X`.

[20] OERTLI J. Cost–Benefit Analysis in Railway Noise Control. Journal of Sound and Vibration. 2000;231(3):505-9. Available from: `https://www.sciencedirect.com/science/article/pii/S0022460X99925397`.

[21] Redondo J, Peiró-Torres MP, Llinares C, Bravo JM, Pereira A, Amado-Mendes P. Correlation between objective and subjective assessment of noise barriers. Applied Acoustics. 2021;172:107640. Available from: `https://www.sciencedirect.com/science/article/pii/S0003682X20307441`.

[22] Lee HP, Lim KM, Kumar S. Noise assessment of elevated rapid transit railway lines and acoustic performance comparison of different noise barriers for mitigation of elevated railway tracks noise. Applied Acoustics. 2021;183:108340. Available from: `https://www.sciencedirect.com/science/article/pii/S0003682X21004345`.

[23] Fiorini CV. Railway noise in urban areas: assessment and prediction on infrastructure improvement combined with settlement development and regeneration in central Italy. Applied Acoustics. 2022;185:108413. Available from: `https://www.sciencedirect.com/science/article/pii/S0003682X21005077`.

[24] Tadeu A, António J, Mendes PA, Godinho L. Sound pressure level attenuation provided by thin rigid screens coupled to tall buildings. Journal of Sound and Vibration. 2007;304(3):479-96. Available from: `https://www.sciencedirect.com/`

science/article/pii/S0022460X07001769.

[25] Duhamel D. Efficient Calculation of the Three-Dimensional Sound Pressure Field around a Noise Barrier. Journal of Sound and Vibration. 1996;197(5):547-71. Available from: https://www.sciencedirect.com/science/article/pii/S0022460X96905489.

[26] Godinho L, António J, Tadeu A. 3D sound scattering by rigid barriers in the vicinity of tall buildings. Applied Acoustics. 2001;62(11):1229-48. Available from: https://www.sciencedirect.com/science/article/pii/S0003682X01000044.

[27] António J, Tadeu A, Mendes PA. A 2.5D Traction boundary element method formulation applied to the study of wave propagation in a fluid layer hosting a thin rigid body. Journal of Computational Acoustics. 2008;16(02):177-98. Available from: https://doi.org/10.1142/S0218396X08003567.

[28] Tadeu A, António J, Godinho L, Amado Mendes P. Simulation of sound absorption in 2D thin elements using a coupled BEM/TBEM formulation in the presence of fixed and moving 3D sources. Journal of Sound and Vibration. 2012;331(10):2386-403. Available from: https://www.sciencedirect.com/science/article/pii/S0022460X12000235.

[29] António J, Tadeu A, Castro I. Performance of double three-dimensional rigid barriers used to create an acoustic space—A normal derivative integral equationapproach. Journal of Sound and Vibration. 2013;332(13):3258-69. Available from: https://www.sciencedirect.com/science/article/pii/S0022460X13000394.

[30] Bordón JDR, Aznárez JJ, Maeso O. A 2D BEM–FEM approach for time harmonic fluid–structure interaction analysis of thin elastic bodies. Engineering Analysis with Boundary Elements. 2014;43:19-29. Available from: https://www.sciencedirect.com/science/article/pii/S0955799714000575.

[31] Toledo R, Aznárez JJ, Maeso O, Greiner D. In: Magalhães-Mendes J, Greiner D, editors. A Procedure for Improving the Acoustic Efficiency of Top-Edge Devices on Noise Barriers: An Application of Genetic Algorithms and Boundary Elements. Cham: Springer International Publishing; 2015. p. 105-25. Available from: https://doi.org/10.1007/978-3-319-20406-2_7.

[32] Toledo R, Aznárez JJ, Greiner D, Maeso O. Shape design optimization of road acoustic barriers featuring top-edge devices by using genetic algorithms and boundary elements. Engineering Analysis with Boundary Elements. 2016;63:49-60. Available from: https://www.sciencedirect.com/science/article/pii/S0955799715002234.

[33] Toledo R, Aznárez JJ, Greiner D, Maeso O. A methodology for the multi-objective shape optimization of thin noise barriers. Applied Mathematical Modelling. 2017;50:656-75. Available from: https://www.sciencedirect.com/science/article/pii/S0307904X17304122.

[34] Li Q, Duhamel D, Luo Y, Yin H. Analysing the acoustic performance of a nearly-enclosed noise barrier using scale model experiments and a 2.5-D BEM approach. Applied Acoustics. 2020;158:107079. Available from: https://www.sciencedirect.com/science/article/pii/S0003682X19303469.

[35] Li X, Hu X, Zheng J. Statistical energy method for noise reduction performance of the vertical noise barrier alongside railway bridges. Applied Acoustics. 2020;170:107503. Available from: https://www.sciencedirect.com/science/article/pii/S0003682X20306071.

[36] Lázaro J, Pereira M, Costa PA, Godinho L. Performance of Low-Height Railway Noise Barriers with Porous Materials. Applied Sciences. 2022;12(6). Available from: https://www.mdpi.com/2076-3417/12/6/2960.

[37] Peake MJ, Trevelyan J, Coates G. Extended isogeometric boundary element method (XIBEM) for two-dimensional Helmholtz problems. Computer Methods in Applied Mechanics and Engineering. 2013;259:93-102. Available from: https://www.sciencedirect.com/science/article/pii/S0045782513000674.

[38] Simpson RN, Scott MA, Taus M, Thomas DC, Lian H. Acoustic isogeometric boundary element analysis. Computer Methods in Applied Mechanics and Engineering. 2014;269:265-90. Available from: https://www.sciencedirect.com/science/article/pii/S0045782513002788.

[39] Liu C, Chen L, Zhao W, Chen H. Shape optimization of sound barrier using an isogeometric fast multipole boundary

element method in two dimensions. Engineering Analysis with Boundary Elements. 2017;85:142-57. Available from: `https://www.sciencedirect.com/science/article/pii/S0955799717300930`.

[40] Jiang F, Zhao W, Chen L, Zheng C, Chen H. Combined shape and topology optimization for sound barrier by using the isogeometric boundary element method. Engineering Analysis with Boundary Elements. 2021;124:124-36. Available from: `https://www.sciencedirect.com/science/article/pii/S0955799720303167`.

[41] Velázquez-Mata R, Romero A, Domínguez J, Tadeu A, Galvín P. A novel high-performance quadrature rule for BEM formulations. Engineering Analysis with Boundary Elements. 2022;140:607-17. Available from: `https://www.sciencedirect.com/science/article/pii/S095579972200145X`.

[42] Zhang X, Jeong H, Thompson D, Squicciarini G. Experimental study of noise mitigation measures on a slab track. Applied Acoustics. 2021;172:107630. Available from: `https://www.sciencedirect.com/science/article/pii/S0003682X20307349`.

[43] Knuth C, Squicciarini G, Thompson D. An efficient model for predicting the sound radiation from a railway rail accounting for cross-section deformation. Journal of Sound and Vibration. 2025;618:119323. Available from: `https://www.sciencedirect.com/science/article/pii/S0022460X25003979`.

[44] Romero A, Galvín P, Cámara-Molina JC, Tadeu A. On the formulation of a BEM in the Bézier–Bernstein space for the solution of Helmholtz equation. Applied Mathematical Modelling. 2019;74:301-19. Available from: `https://www.sciencedirect.com/science/article/pii/S0307904X19302720`.

[45] Romero A, Tadeu A, Galvín P, António J. 2.5D coupled BEM–FEM used to model fluid and solid scattering wave. International Journal for Numerical Methods in Engineering. 2015;101(2):148-64. Available from: `https://onlinelibrary.wiley.com/doi/abs/10.1002/nme.4801`.

[46] Tadeu AJB, Kausel E. Green's Functions for Two-and-a-Half-Dimensional Elastodynamic Problems. Journal of Engineering Mechanics. 2000;126(10):1093-7.

[47] Cruz-Muñoz FJ, Romero A, Galvín P, Tadeu A. Acoustic waves scattered by elastic waveguides using a spectral approach with a 2.5D coupled boundary-finite element method. Engineering Analysis with Boundary Elements. 2019;106:47-58. Available from: `https://www.sciencedirect.com/science/article/pii/S0955799718307732`.

[48] Thompson DJ, Zhao D, Ntotsios E, Squicciarini G, Cierco E, Jansen E. The influence of reflections from the train body and the ground on the sound radiation from a railway rail. Railway Sciences. 2024;3(1):1-17. Available from: `https://doi.org/10.1108/RS-11-2023-0041`.

[49] Wu TW. Boundary Element Acoustics Fundamentals and Computer Codes. Advances in Boundary Elements. WIT Press; 2000.

[50] Nilsson CM, Jones CJC, Thompson DJ, Ryue J. A waveguide finite element and boundary element approach to calculating the sound radiated by railway and tram rails. Journal of Sound and Vibration. 2009;321(3):813-36. Available from: `https://www.sciencedirect.com/science/article/pii/S0022460X08008754`.

[51] Sun W, Thompson D, Toward M, Zeng Z. Modelling of vibration and noise behaviour of embedded tram tracks using a wavenumber domain method. Journal of Sound and Vibration. 2020;481:115446. Available from: `https://www.sciencedirect.com/science/article/pii/S0022460X20302789`.

[52] Renfe. S-103: Flota de trenes; n.d. Accessed: April 2025. `https://www.renfe.com/es/es/grupo-renfe/grupo-renfe/flota-de-trenes/s-103`.